Highly efficient visible-light driven solar-fuel production over tetra(4-carboxyphenyl)porphyrin iron(III) chloride using CdS/Bi$_2$S$_3$ heterostructure as photosensitizer

Pan Li[a,c], Xuehua Zhang[a,c,*], Chunchao Hou[b], Yong Chen[b,c,*], Tao He[a,c,*]

[a] CAS Key Laboratory of Nanosystem and Hierarchical Fabrication, CAS Center for Excellence in Nanoscience, National Center for Nanoscience and Technology, Beijing 100190, China
[b] Key Laboratory of Photochemical Conversion and Optoelectronic Materials, Technical Institute of Physics and Chemistry, Chinese Academy of Sciences, Beijing 100190, China
[c] University of Chinese Academy of Sciences, Beijing 100049, China

ARTICLE INFO

ABSTRACT

Fabrication of hybrid system coupling inorganic semiconductor photosensitizer with molecular catalyst provides a promising approach to achieve highly efficient CO$_2$ reduction into solar fuels, as the semiconductor nanomaterials can meet the prerequisites of visible-light photoresponse and high charge-separation efficiency for achieving high photocatalytic efficiency. In this work, CdS/Bi$_2$S$_3$ heterostructures have been prepared *via* an ion-exchange reaction and employed as the photosensitizer to couple with tetra(4-carboxyphenyl)porphyrin iron(III) chloride (FeTCPP) molecular catalyst for photoreduction of CO$_2$ into CO and H$_2$ under visible-light irradiation. The sulfur vacancy in CdS surface can be reduced by the formation of CdS/Bi$_2$S$_3$ heterostructure. The content of Bi$_2$S$_3$ can be modulated *via* tailoring the ion-exchange reaction time. The resulting effect on the performace of CO$_2$ photoreduction has been investigated in detail. Benefiting from the enhanced separation and utilization of charge carriers, CdS/Bi$_2$S$_3$-0.5 h/FeTCPP hybrid catalyst exhibits 8.2 times CO yield (1.93 mmol/g/h) and 1.7 times H$_2$ yield (6.08 mmol/g/h) of CdS/FeTCPP hybrid catalyst. More important, the results of energy level alignment, electron spin resonance and photocatalysis indicate that electron-transfer direction can be changed once the CdS/Bi$_2$S$_3$ heterostructure is coupled with FeTCPP. In the CdS/Bi$_2$S$_3$ heterostructure, electrons transfer mainly from the conduction band of CdS to Bi$_2$S$_3$, while it is mainly from the conduction band of CdS to FeTCPP in the CdS/Bi$_2$S$_3$/FeTCPP hybrid.

1. Introduction

Photocatalytic reduction of CO$_2$ into value-added solar fuels has been the focus of active research as it may simultaneously address future energy supply and mitigate carbon emission [1–11]. However, CO$_2$ reduction is a highly energy-demanding process, whereas a negative potential of –1.90 V (*vs* normal hydrogen electrode, NHE) is required for the formation of initial intermediate CO$_2^-$ *via* one-electron reduction. A more favorable pathway to reduce CO$_2$ is *via* proton-assisted multiple-electron transfer process. Molecular catalysts with high activity have gained much attention owing to their multiple and accessible redox states, which are favorable of the multi-electron transfer process for CO$_2$ reduction [12–15]. Nevertheless, it is still very challenging to develop highly efficient molecular catalysts due to their

intrinsic unstability and low visible-light harvesting. Given the superior durability and light-harvesting ability of inorganic semiconductors, the hybrid systems integrating semiconductors with molecular catalysts can take advantage of both the molecular catalysts and inorganic semiconductors [16–21]. In such a hybrid system, the semiconductor acts as the light absorber to generate electrons and holes, and the molecular catalyst serves as the catalytic center for the reduction reaction. Therefore, efficient charge separation and utilization in a hybrid system are critical for achieving highly photocatalytic performance.

CdS is a traditional II−VI semiconductor with a narrow band gap of 2.4 eV, possessing good visible-light absorption and very negative conduction band potential (E_{CB}), which can be used as the visible-light driven photocatalyst [22–25]. However, CdS suffers from severe recombination of photogenerated electrons and holes [26]. The formation

---

* Corresponding authors at: CAS Key Laboratory of Nanosystem and Hierarchical Fabrication, CAS Center for Excellence in Nanoscience, National Center for Nanoscience and Technology, Beijing 100190, China.
E-mail addresses: zhangxh@nanoctr.cn (X. Zhang), chenyong@mail.ipc.ac.cn (Y. Chen), het@nanoctr.cn (T. He).

of heterostructure through coupling with a narrow band gap semiconductor can not only improve the charge separation efficiency, but also further enhance the visible-light harvesting. As a narrow band gap (1.3–1.7 eV) semiconductor, Bi_2S_3 has been considered a good material to combine with CdS to improve the photocatalytic activity [27]. Much effort has been devoted to CdS/Bi_2S_3 heterostructure in photocatalysis, such as organic dye degradation, H_2 evolution, and CO_2 photoreduction [28–30]. Moreover, it is aware of that the combination of CdS/Bi_2S_3 heterostructure with molecular catalysts can further improve the activity of CO_2 photoreduction, albeit the corresponding charge transfer mechanism is still not well understood. In addition, iron porphyrin-based molecular catalysts have been used as electro- and photo-catalysts for CO_2 reduction owing to its relatively high activity and stability, earth abundant, and environmentally benign nature [31–34]. However, most of the iron porphyrins are inactive for CO_2 reduction under visible-light irradiation if not combining with the suitable photo-sensitizers [33,34].

Herein we prepared CdS/Bi_2S_3 heterostructures *via* a simple ion-exchange reaction, which was combined with tetra(4-carboxyphenyl) porphyrin iron(III) chloride (FeTCPP) to fabricate hybrid catalysts ($CdS/Bi_2S_3/FeTCPP$) for photoreduction of CO_2 into solar fuels (CO and H_2) under visible-light irradiation. In such a heterogeneous hybrid catalyst, CdS/Bi_2S_3 heterostructure works as the light-harvesting unit and FeTCPP acts as the catalytic center. The construction of CdS/Bi_2S_3 heterostructure is in favor of the charge separation and utilization. The obtained $CdS/Bi_2S_3/FeTCPP$ catalysts exhibit higher yield for both CO and H_2 evolution than CdS/FeTCPP hybrid catalyst. The corresponding charge transfer mechanism has been systematically studied.

2. Experimental methods

2.1. Chemicals

All of the chemicals and solvents used in this work were analytical or chromatographic grade. $Cd(NO_3)_2 \cdot 4H_2O$ was bought from Shanghai Macklin Biochemical Technology Co., Ltd. $CS(NH_2)_2$ was obtained from Jingke Fine Chemical Industry Research Institute of Tianjin. Ethylene glycol (EG) was purchased from Xilong Scientific Co., Ltd. $Bi(NO_3)_3 \cdot 5H_2O$ was bought from Alfa Aesar. Triethanolamine (TEOA, 99.8%, GC), acetonitrile (MeCN, 99.9%, GC) and ethylenediamine (> 99%) were purchased from Shanghai Aladdin Bio-Chem Technology. Carbon dioxide gas (CO_2, super grade purity 99.999%) was bought from Beijing Beiwen Gases Company. 5,5dimethylpyrroline *N*oxide (DMPO) was got from Dojindo Laboratories, Japan. The high-purity water was acquired from a Milli-Q Plus system (Millipore, France) with 18.2 MΩ cm resistivity.

2.2. Synthesis of CdS nanorods, CdS/Bi_2S_3 heterostructures and FeTCPP

CdS nanorods were synthesized *via* solvothermal route using ethylenediamine as solvent and structure-directing agent. In a typical process, 3 mmol $Cd(NO_3)_2 \cdot 4H_2O$ and 9 mmol $CS(NH_2)_2$ were dissolved in 30 ml of the mixture of ethylenediamine and water (v:v = 2:1) under constant stirring for 30 min. Then the obtained mixture was transferred into an autoclave and maintained at 180 °C for 12 h in a muffle furnace. The resultant yellow precipitate was separated by centrifugation after being cooled down to the room temperature, then washed with ethanol and high-purity water for several times, and finally dried overnight in a vacuum oven at 65 °C, which is denoted as CdS.

The CdS/Bi_2S_3 heterostructures were synthesized *via* a simple ion-exchange reaction in EG solution. Briefly, 0.5 mmol as-synthesized CdS nanorods were dispersed in 20 ml of EG under ultrasonication for 15 min. Then 1.5 mmol $Bi(NO_3)_3$ in 20 ml of EG was added dropwise into the above mixture and was maintained at 75 °C with constant stirring for different times (0.5 h, 1 h and 2 h). The resultant products were collected by centrifugation, followed by being washed with high-

purity water and absolute ethanol for several times. Finally, the obtained samples were dried in vacuum at 65 °C overnight. The samples are respectively denoted as CdS/Bi_2S_3-0.5 h and CdS/Bi_2S_3-1 h according to the reaction time; while the one after 2-h reaction is Bi_2S_3 since all the CdS was converted.

FeTCPP was synthesized according to the protocol reported previously [34,35].

2.3. Characterizations

The morphology, chemical composition and element mapping analysis were achieved by using Hitachi S4800 field emission scanning electron microscope (FE-SEM) and Tecnai G2 F20 U-TWIN transmission electron microscopy (TEM). Powder X-ray diffraction (XRD) was performed on a Bruker D8 diffractmeter with Cu Kα radiation. X-ray photoelectron spectroscopy (XPS) was carried out on ESCALAB 250Xi X-ray photoelectron spectrometer. UV–vis diffuse reflectance spectroscopy (DRS) and UV–vis absorption spectra were collected on a Lambda 750 UV/Vis/NIR spectrophotometer (Perkin-Elmer, USA) using $BaSO_4$ as background. The BET specific surface area and CO_2 adsorption isotherms were obtained by a surface area and porosity analyzer (Micromeritics, Tristar II 3020).

Photoluminescence (PL) spectra excited at 350 nm were collected on FLS980 spectrometer (Edinburgh Instruments Ltd.). Time-resolved PL spectra were recorded with 375 nm excitation. Electron spin resonance (ESR) spectra were obtained with a Bruker E500 spectrometer at room temperature. The Mott-Schottky and transient photocurrent response curves were performed in a three-electrode cell on CHI 660D electrochemical station (Shanghai Chenhua) with a frequency of 1 kHz. The as-prepared samples, Pt plate and saturated calomel electrode (SCE) were used respectively as the working, counter and reference electrodes. For convenience, the potential was converted to that *vs* NHE.

2.4. Photocatalytic reduction of CO_2

CO_2 photoreduction experiments were performed in a photoreaction system (Labsolar-IIIAG, Beijing Perfect Light Technology Co., Ltd.) saturated with 29 kPa CO_2 at 15 °C [34]. Briefly, 1 mg of FeTCPP molecular catalyst and 50 mg of CdS/Bi_2S_3 powder were suspended in 100 ml solution of acetonitrile/water/TEOA (3:1:1, v:v:v) under constant stirring. The system was first vacuumed and then purged with Ar for at least 1 h to ensure the removal of residual air. Before illumination, the system was purged with high purity CO_2 gas in the dark for at least 1.5 h. The reactor was illuminated by a 300 W Xe lamp (Microsolar 300, Beijing Perfect Light Technology Co., Ltd.) with a 420-nm cut-off filter and an IR cut-off filter. The intensity of resultant visible light was 260 mW cm^{-2}. The gas products were analyzed by using Agilent 7890 A gas chromatography equipped with a hydrogen flame ionized detector (FID) and a thermal conductivity detector (TCD). Four control experiments (*i.e.*, without CO_2 purging, without illumination, blank solvent without photocatalysts, and only FeTCPP catalyst) were carried out to ensure that CO_2 is the only carbon source for any observed products.

3. Results and discussion

3.1. Structure, morphology and composition of CdS, Bi_2S_3 and CdS/Bi_2S_3

Crystal structure and composition of the as-prepared samples are investigated by XRD. Fig. 1 shows XRD patterns of the CdS/Bi_2S_3 heterostructures, as well as pure CdS and Bi_2S_3 samples. The diffraction peaks of pure CdS are well ascribed to hexagonal Wurtzite phase CdS (JCPDS: 41–1049). After the ion-exchange reaction with Bi^{3+} for 0.5 h, the peaks assigned to the orthorhombic Bi_2S_3 (JCPDS: 17-0320) can be observed. CdS provides S source and acts as the matrices crystal during the ion-exchange reaction, which dissolves gradually; while Bi^{3+} reacts
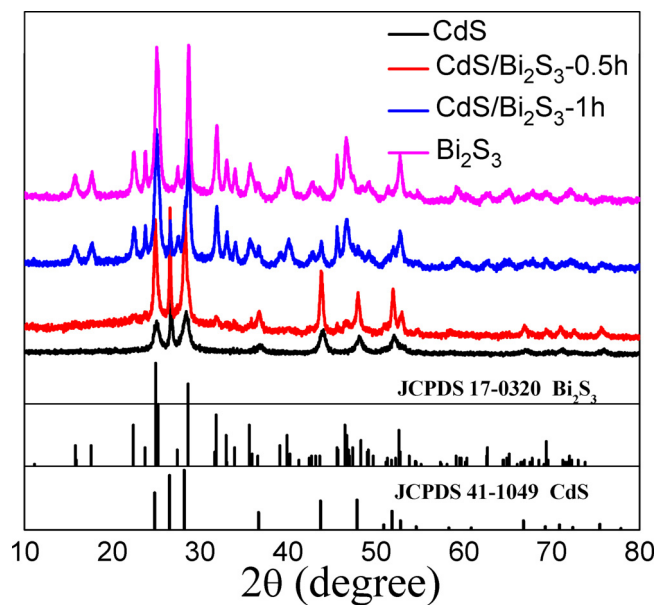
Fig. 1. The XRD patterns of the synthesized CdS, Bi_2S_3 and CdS/Bi_2S_3 heterostructures.

Table 1
The elemental composition of the as-synthesized samples derived from EDX analysis.

Sample	CdS	CdS/Bi$_2$S$_3$-0.5h	CdS/Bi$_2$S$_3$-1h	Bi$_2$S$_3$
S (at.%)	4.02	4.07	2.49	5.41
Cd (at.%)	3.74	2.93	0.45	0.00
Bi (at.%)	0.00	0.69	1.40	3.63
(S-Cd)/Bi[a]		1.65	1.46	1.49
Bi$_2$S$_3$/CdS		0.12	1.55	

[a] Here (S—Cd) means the amount of S connected with Bi.

with the already-existing S source and recrystallizes to form Bi_2S_3 on the CdS surface due to its extremely lower solubility ($K_{sp} = 1 \times 10^{-97}$) than CdS ($K_{sp} = 8 \times 10^{-27}$) [29,36]. It is found that the intensity of diffraction peaks for Bi_2S_3 increases as the reaction time prolongs. When the reaction time is extended to 2 h, the peaks for CdS disappear and all the observed peaks are ascribed to the orthorhombic Bi_2S_3, implying that CdS has been completely transformed into Bi_2S_3. During the synthesis of CdS/Bi_2S_3 heterostructures, the EG was chosen as the solvent mainly because $Bi(NO_3)_3$ is easily hydrolyzed in aqueous solution, while it can be successfully dissolved in EG to form Bi^{3+} ions. In addition, EG can slow down the rate of ion-exchange reaction by virtue of the low polarity and large viscosity.

Fig. 2 shows FE-SEM images of the as-synthesized CdS, Bi_2S_3 and CdS/Bi_2S_3 samples. Pure CdS has the nanorod morphology (Fig. 2a). After 0.5 h of ion-exchange reaction with Bi source, no obvious change in morphology can be observed (Fig. 2b), although little Bi_2S_3 has been formed. If further increasing the ion-exchange reaction time to 1 h, CdS continues to transform into Bi_2S_3, and interestingly, the surface of nanorods becomes slightly smoother and more uniform than before (Fig. 2c). Finally, pure Bi_2S_3 nanorods with uniform morphology are obtained (Fig. 2d). Elemental composition of the obtained samples was checked from EDX analysis and listed in Table 1. The Cd and S atoms are detected in pure CdS, for which the atomic ratio is close to 1. The element Bi can be detected after the ion-exchange reaction with Bi^{3+} for 0.5 h, for which the ratio of (S—Cd)/Bi is calculated to be around 1.5, indicating the formation of Bi_2S_3. The resultant molar ratio of Bi_2S_3/CdS is around 0.12 for CdS/Bi_2S_3-0.5 h. The amount of Bi_2S_3 increases with prolonging the ion-exchange reaction time. The molar ratio of Bi_2S_3/CdS is around 1.55 for CdS/Bi_2S_3-1 h, and pure Bi_2S_3 is obtained when the ion-exchange reaction time increases to 2 h. All these are in good agreement with the aforementioned XRD results.

Fig. 3 shows TEM images, SAED pattern, and line-scan composition profiles taken along the radial and axial directions of CdS and CdS/Bi_2S_3-0.5 h, respectively. TEM image further verifies the nanorod morphology of CdS (Fig. 3a). The SAED pattern (inset of Fig. 3b) indicates the single-crystalline nature of CdS nanorods. The line-scan composition analysis taken along the radial (Fig. 3c) and axial
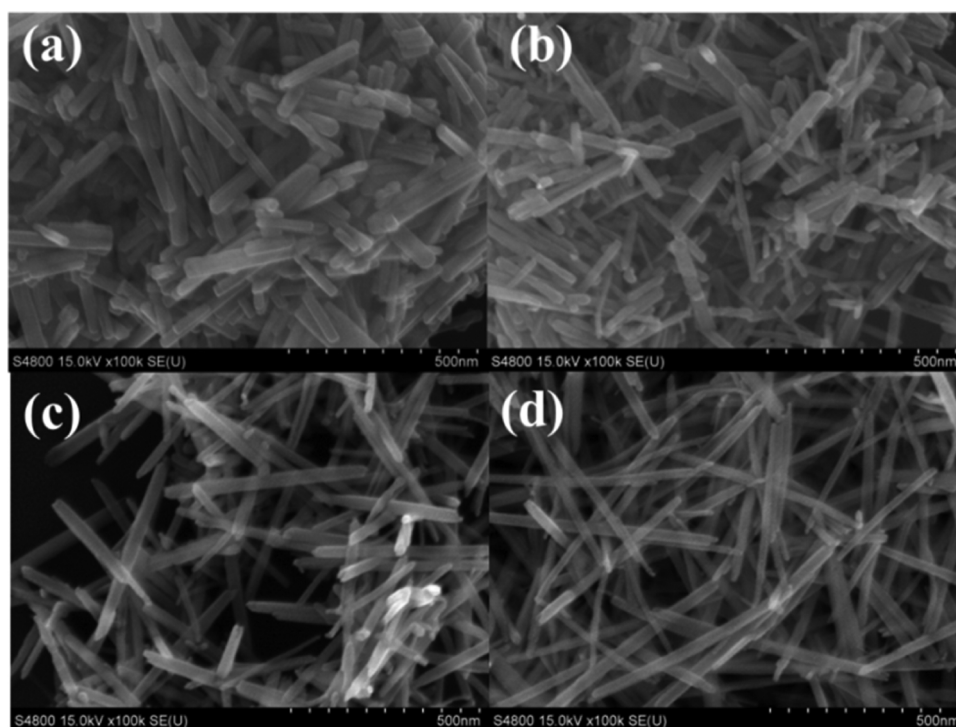

Fig. 2. SEM images of the as-synthesized samples, (a) CdS nanorods, (b) CdS/Bi$_2$S$_3$-0.5h, (c) CdS/Bi$_2$S$_3$-1h, and (d) Bi$_2$S$_3$.
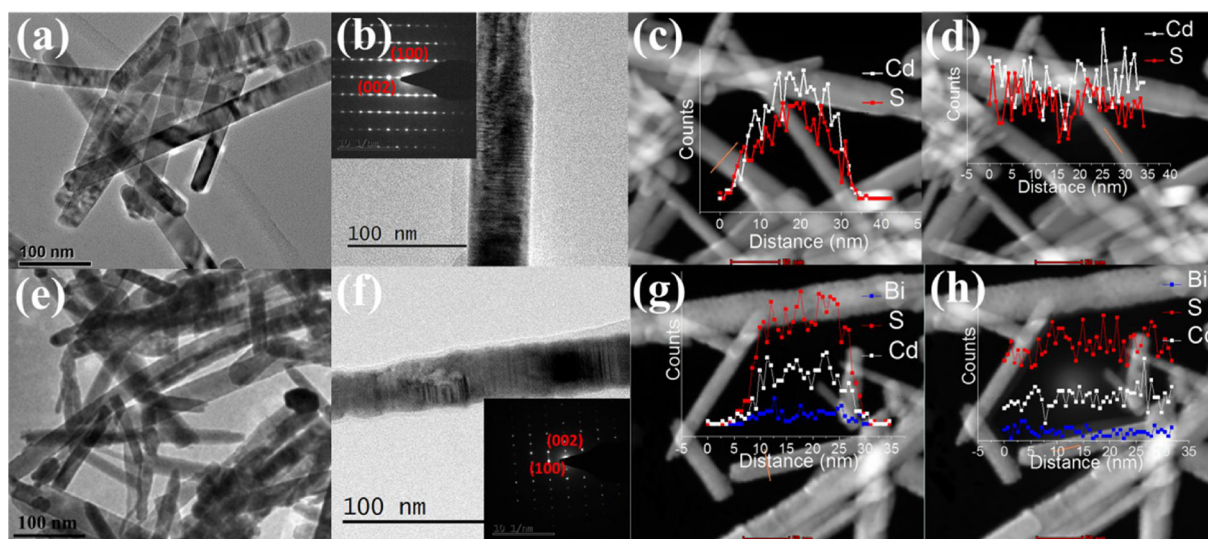
Fig. 3. (a, e) TEM images, (b, f) SAED patterns, and line-scan composition profiles taken along the (c, g) radial and (d, h) axial directions of (a–d) CdS and (e–h) CdS/Bi_2S_3-0.5h heterostructure, respectively.

directions (Fig. 3d) reveal that the nanorods are composed of Cd and S elements, which are distributed homogeneously. The nanorod morphology and single-crystalline nature are still well maintained after 0.5 h of ion-exchange reaction (Fig. 3e and f). Meanwhile, the Bi element can be detected from line-scan composition analysis (Fig. 3g and h), although the content is still low. If further increasing the ion-exchange reaction time, as shown in Fig. S1 for CdS/Bi_2S_3-1 h sample, the content of Cd decreases while Bi increases, suggesting that the transformation of CdS to Bi_2S_3. When the ion-exchange reaction time reaches 2 h, only Bi and S elements can be detected from the line-scan composition results (Fig. S2), indicating the complete transformation of CdS to Bi_2S_3, which is well consistent with the above XRD and EDX analysis from SEM. In addition, the typical N_2 adsorption-desorption isotherms of CdS, Bi_2S_3 and CdS/Bi_2S_3 heterostructures are displayed in Fig. S3. The corresponding BET specific surface area is determined to be 27.97, 33.43, 25.08 and 26.84 m^2/g for CdS, CdS/Bi_2S_3-0.5h, CdS/Bi_2S_3-1h and Bi_2S_3, respectively.

The chemical composition of the as-synthesized samples were further analyzed by XPS. The survey spectra in Fig. 4a clearly indicate that the obtained samples are composed of Cd, S, and/or Bi elements. The high-resolution XPS spectra of Bi4f (Fig. 4b) shows two peaks at binding energy of 163.6 and 158.3 eV, corresponding to $Bi4f_{5/2}$ and $Bi4f_{7/2}$, respectively. The doublet peak separation between the $Bi4f_{5/2}$ and $Bi4f_{7/2}$ is 5.3 eV, indicating that the valence state of Bi is +3 [28]. The peaks at around 162.3 and 161.1 eV are ascribed to $S2p_{1/2}$ and $S2p_{3/2}$, respectively. The resultant splitting energy of ~1.2 eV is the characteristic value of S^{2-} [29]. As for the high resolution XPS spectra of Cd3d (Fig. 4c), two peaks at about 411.5 and 404.8 eV can be assigned to $Cd3d_{3/2}$ and $Cd3d_{5/2}$, respectively. The splitting energy of 6.7 eV between $Cd3d_{3/2}$ and $Cd3d_{5/2}$ is a typical value for Cd^{2+} in sulfides [37]. The shift of Cd3d to a higher binding energy for the Bi_2S_3/CdS heterostructures is due to the interaction between Bi_2S_3 and CdS.

3.2. Determination of energy levels

UV-visible absorption spectra show that CdS possesses an absorption edge around 530 nm and Bi_2S_3 exhibits strong absorption in the whole UV–vis region (Fig. 5a). The two fluctuations at around 500 nm and 860 nm in Fig. 5a are due to the lamp change of the spectrophotometer during measurements. Obviously, CdS/Bi_2S_3 heterostructures can extend the light absorption edge up to about 1000 nm, covering the full visible-light and part IR range. The band gap (E_g) of the pure CdS and Bi_2S_3 samples can be estimated from the absorption spectra based on

the Kubelka-Munk method, as depicted respectively in Fig. 5b and c. The E_g of CdS is calculated to be 2.44 eV, and Bi_2S_3 has a relatively narrow E_g of 1.52 eV.

To evaluate the band structure of the as-synthesized CdS and Bi_2S_3 samples, Mott-Schottky plots were measured to determine the Flat-band potential (E_{FB}) using equation (1), where C is space charge capacitance, N_D is donor density, ε and ε_0 are the respective dielectric constants of free space and film electrode, E is applied potential, E_{FB} is flat-band potential, K_B is Boltzmann's constant, T is temperature, and q is electronic charge [38].

$$\frac{1}{C^2} = \frac{2}{\varepsilon\varepsilon_0 N_D}\left(E - E_{FB} - \frac{K_B T}{q}\right) \tag{1}$$

Fig. S4 shows the Mott-Schottky plots of CdS and Bi_2S_3. Positive slope of the linear section in the Mott-Schottky plots indicates the n-type behavior of CdS and Bi_2S_3. The E_{FB} value can be estimated from the interception at X axis by linear extrapolating the linear region (1/$C^2 = 0$), which is –1.52 and –0.42 V (*vs* SCE) for CdS and Bi_2S_3, equivalent to –1.28 and –0.18 V (*vs* NHE), respectively. It is known that the CB position (E_{CB}) of an n-type semiconductor is 0.1–0.3 eV higher than E_{FB}, dependent on the electron effective mass and carrier concentration [39]. Here, the voltage difference between E_{CB} and E_{FB} is set to be 0.2 eV, and thereby, the bottom of the E_{CB} for CdS and Bi_2S_3 is –1.48 and –0.38 V (*vs* NHE), respectively. The reduction potential of FeTCPP is −1.02 V (*vs* NHE), thus electron transfer from the CB of CdS to FeTCPP is thermodynamically feasible, while the electron transfer from the CB of Bi_2S_3 to FeTCPP is thermodynamically unfavorable [34]. Combining with the E_g derived from the absorption spectra in Fig. 5, in addition, the valence band value (E_{VB}) is calculated to be 0.96 V and 1.14 V (*vs* NHE) for CdS and Bi_2S_3, respectively.

3.3. Photoreduction of CO_2 over heterogeneous hybrid catalysts

A series of control experiments were first carried out, *i.e.*, without CO_2 purging, without illumination, blank solvent without the photocatalysts, and only FeTCPP molecular catalyst. No any products like CH_4 or CO can be detected in these experiments, indicating that the observed products indeed come from the CO_2 photoreduction. For pure FeTCPP under visible-light irradiation, it is because of the lack of light absorber that there is no any reduction products observed.

Fig. 6 shows the CO_2 photoreduction results using the as-prepared semiconductor as light harvesting unit and FeTCPP as the catalyst
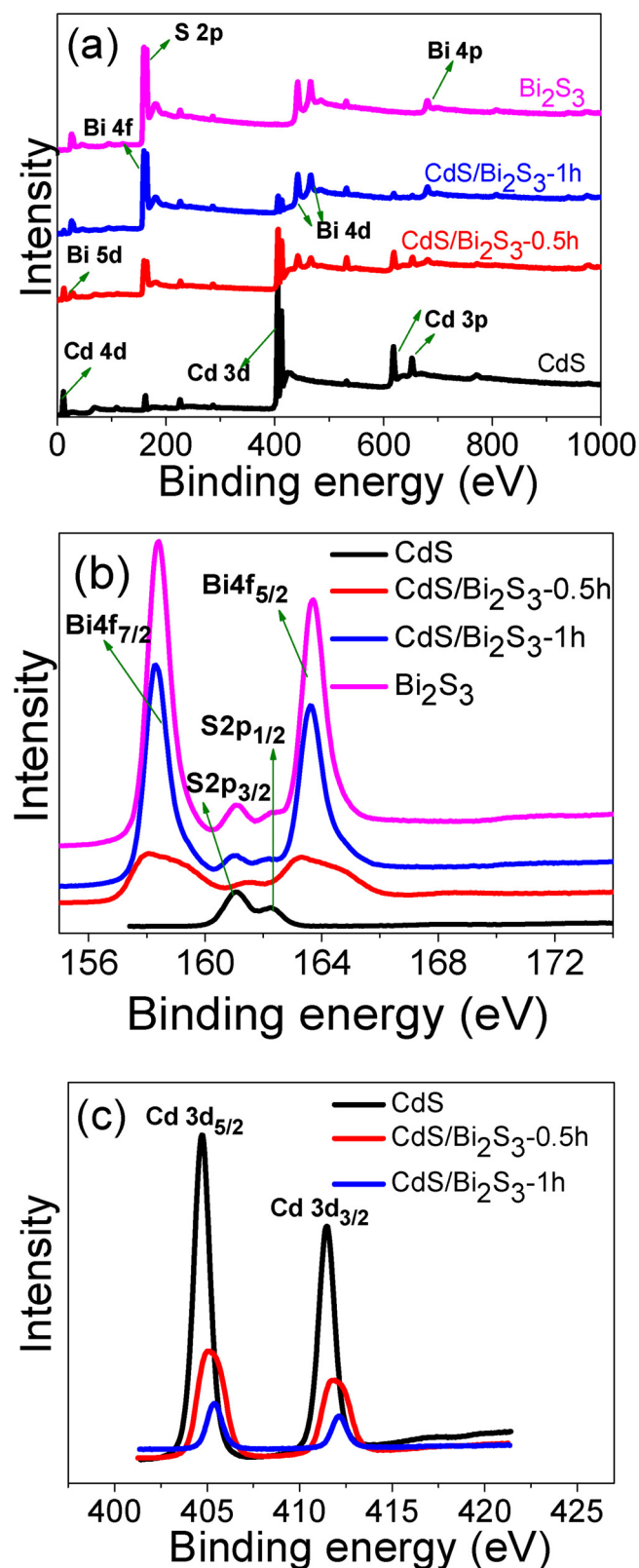
Fig. 4. XPS spectra of (a) survey, (b) Bi4f and S2p, and (c) Cd3d of the as-synthesized samples.

Fig. 5. (a) UV–vis absorption spectra of the as-synthesized samples, Tauc plots of the as-synthesized (b) CdS and (c) Bi_2S_3 samples.

center under visible-light illumination. Here the amount of FeTCPP is used to calculate the product yield since it acts as the catalytic center. The CO yield is 0.94 mmol/g over the CdS/FeTCPP hybrid catalyst after 4-h visible-light illumination (*i.e.*, ~0.24 mmol/g/h) with trace amount of CH_4 (0.030 μmol); while the CO yield increases to 7.73 mmol/g over
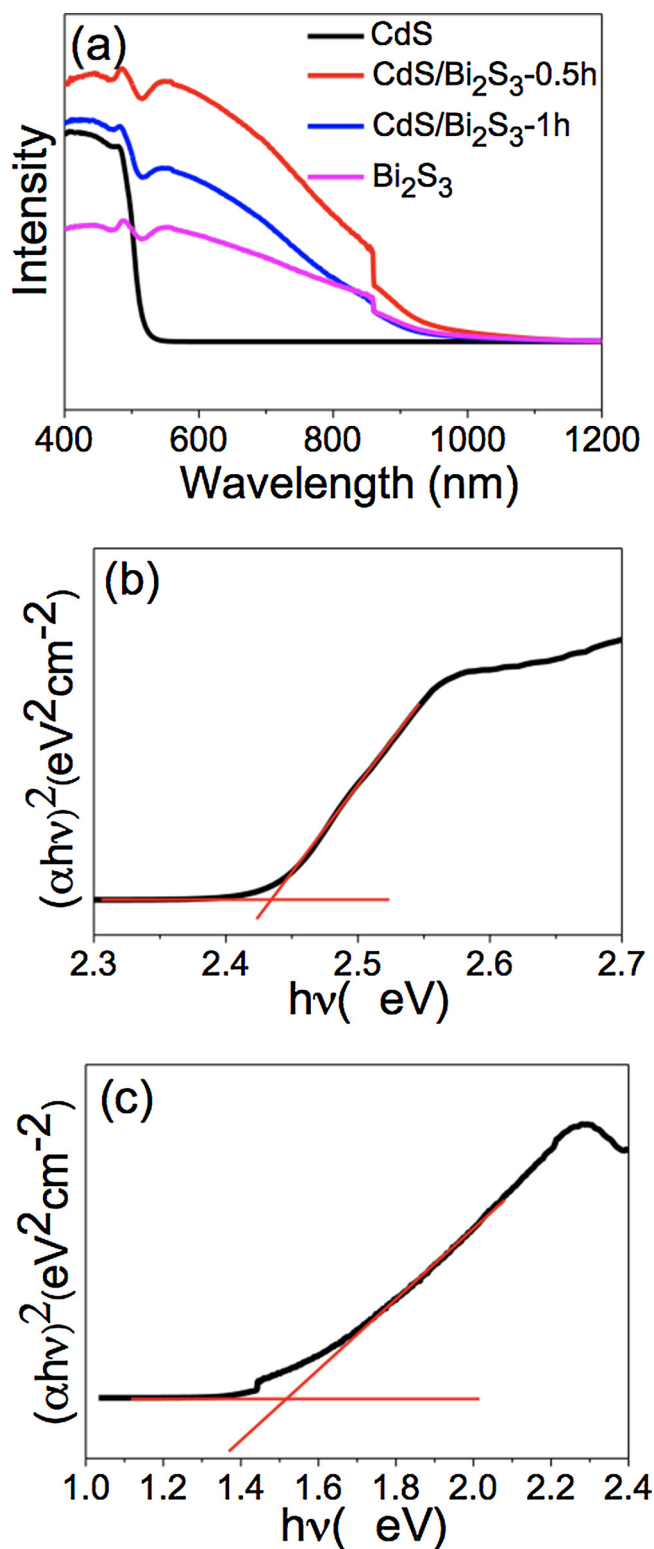
the CdS/Bi_2S_3-0.5 h/FeTCPP hybrid catalyst after 4 h (*i.e.*, 1.93 mmol/g/h) with trace amount of CH_4 (0.040 μmol). That is to say, the CO yield over CdS/Bi_2S_3-0.5 h/FeTCPP is about 8.2 times of that over CdS/FeTCPP. In addition, CO_2 photoreduction using pure CdS and CdS/Bi_2S_3-0.5 h heterostructure as the photocatalyst has been also performed (Table S1). If these results are compared with those acquired over the systems combined with FeTCPP, although not reasonable since
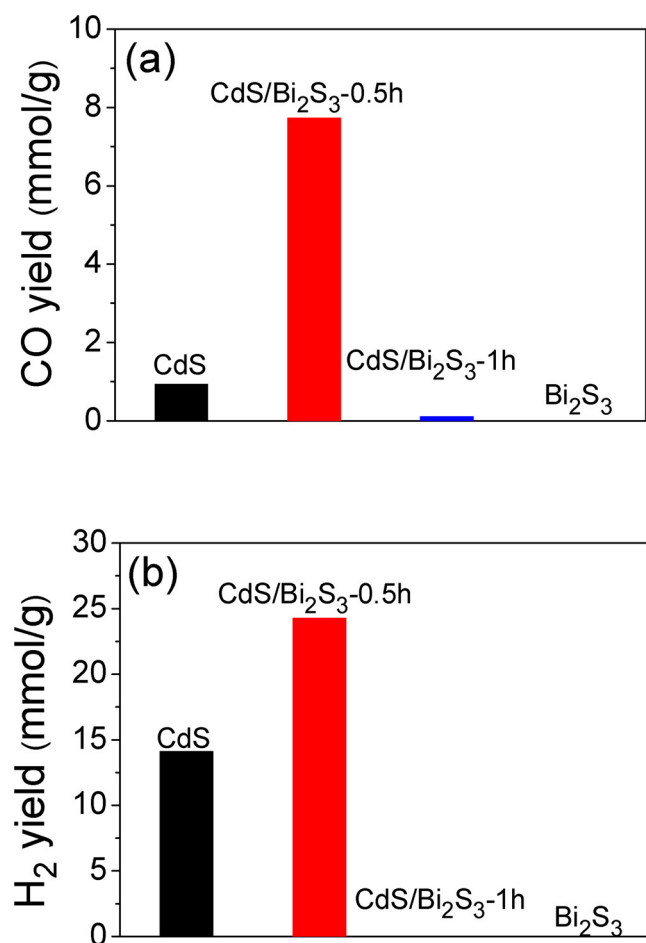
Fig. 6. CO_2 photoreduction over as-synthesized samples coupled with FeTCPP in $CH_3CN:H_2O:TEOA$ (3:1:1, 100 mL) mixed solution after 4-h visible-light illumination (420 nm < λ < 780 nm), light intensity of 260 mW cm^{-2}. As shown in the plots, no CO or H_2 is observed over Bi_2S_3, neither H_2 for CdS/Bi_2S_3-1h.

the active centers are different, the CO yield is much higher for the CdS/FeTCPP catalyst than the pure CdS, and the CH_4 yield is slightly increased for the hybrid catalyst. The same trend is observed for CdS/Bi_2S_3-0.5 h/FeTCPP and CdS/Bi_2S_3-0.5 h catalysts.

Meanwhile, H_2 evolution is also observed mainly due to the in-situ generation of protonated TEOA [TEOA$^+$, *i.e.* $(HOCH_2CH_2)_3NH^+$)], which is an acid with pK_A of about 7.8. This species is in favor of the formation of the porphyrin hydride, eventually leading to the evolution of H_2 [40]. The H_2 yield over the CdS/FeTCPP and CdS/Bi_2S_3-0.5 h/ FeTCPP after 4-h visible-light illumination is 14.12 and 24.30 mmol/g (*i.e.*, 3.53 and 6.08 mmol/g/h), respectively. The latter is about 1.7 times of the former. So CdS/Bi_2S_3-0.5 h/FeTCPP exhibits much higher photoreduction activity than CdS/FeTCPP. However, it is noted that the CdS/Bi_2S_3-1 h/FeTCPP catalyst shows much lower activity than CdS/ Bi_2S_3-0.5 h/FeTCPP, as only very little CO (0.10 mmol/g) and trace amount of CH_4 (0.014 μmol) are detected.

No H_2 or CO is detected over Bi_2S_3/FeTCPP hybrid catalyst, and only trace amount of CH_4 (0.036 μmol) is observed after 4-h visible-light illumination. This should be due to the low E_{CB} (–0.38 V, *vs* NHE) of Bi_2S_3, which can not drive electron transfer from the CB of Bi_2S_3 to FeTCPP (–1.02 V, *vs* NHE). This may be further confirmed by the fact that Bi_2S_3 has very similar CH_4 yield to Bi_2S_3/FeTCPP (Table S1). The photoreduction of CO_2 over CdS/Bi_2S_3-0.5 h/FeTCPP hybrid catalyst performed under illumination with λ > 580 nm can further support this conclusion. In this condition, only trace amount of CH_4 (0.016 μmol) is obtained since Bi_2S_3 can be excited while CdS has no absorption (Fig. 5a) and thus cannot be excited, indicating that the

photoexcited electrons in Bi_2S_3 can transfer neither to the CB of CdS nor to FeTCPP because of its low E_{CB} level (*i.e.*, high electron affinity). The activity of CH_4 production is not discussed since only trace amout of CH_4 is observed upon CO_2 photoreduction over different catalysts.

Two major reasons may account for the enhanced performance of CdS/Bi_2S_3-0.5 h/FeTCPP hybrid catalyst. One is that the amount of surface defects on CdS nanorods can be reduced *via* the ion-exchange reaction, which can be proved by the ESR characterization. As shown in Fig. S5, the typical sulfur vacancy signal appears at g = 2.003 [41]. CdS shows the highest ESR signal, followed by CdS/Bi_2S_3-0.5h and CdS/ Bi_2S_3-1h, indicating that sulfur vacancy content gradually decreases after the formation of CdS/Bi_2S_3 heterojunction. The surface vacancy defects can act as the recombination centers of free electrons and holes. Thus, the decreased sulfur vacancy means that the separation and utilization of the charge carriers can be enhanced. Another possible reason is that the formation of CdS/Bi_2S_3 heterostructure can improve the charge separation efficiency too, as being discussed in the following section. As a result, CdS/Bi_2S_3-0.5h/FeTCPP hybrid photocatalyst shows high CO_2 reduction activity due to the synergistic effect of the enhanced charge separation and utilization. For CdS/Bi_2S_3-0.5h heterostructure, just little Bi_2S_3 is formed on the CdS surface since the molar ratio of Bi_2S_3/CdS is only 0.12 for CdS/Bi_2S_3-0.5h, which means that most of the CdS can still directly hybrid with FeTCPP and the electrons in the CB of CdS can efficiently transfer to FeTCPP. However, most of the CdS is transformed into Bi_2S_3 if further increasing the ion-exchange reaction time (for instance, the molar ratio of Bi_2S_3/CdS is 1.55 for CdS/Bi_2S_3-1h), leaving CdS heavily coated with Bi_2S_3 layer. It is almost impossible for the electrons produced in such heavily-coated CdS transfer to FeTCPP molecular catalyst, resulting in greatly decreased photocatalytic activity of CdS/Bi_2S_3-1h/FeTCPP hybrid catalyst.

In addition, CdS/Bi_2S_3-0.5h/FeTCPP hybrid catalyst exhibits good stability according to the linear increase of the CO and H_2 yield over CdS/Bi_2S_3-0.5h/FeTCPP upon CO_2 reduction under visible-light illumination for 9 h (Fig. S6). Moreover, this is further confirmed by XRD results that the XRD patterns after CO_2 photoreduction (Fig. S7) are similar to those before the photoreduction (Fig. 1).

3.4. Charge transfer mechanism for CO_2 photoreduction

To investigate the charge transfer mechanism, ESR spectra of CdS, CdS/Bi_2S_3-0.5 h and Bi_2S_3 were collected using DMPO as radical scavenger under visible-light illumination. DMPO can react with superoxide radical $\cdot O_2^-$ or carbon-centered radical $-C\cdot$ to form DMPO-radical complex, giving rise to special ESR signals [42–44]. If without TEOA and FeTCPP, a strong characteristic peak of DMPO-$\cdot O_2^-$ with a standard intensity ratio of 1:1:1:1:1 can be observed for pure CdS (Fig. 7a) [42]. Since the redox potential of $O_2/\cdot O_2^-$ is –0.33 V (*vs* NHE), it is very easy for CdS to trap molecular oxygen to generate $\cdot O_2^-$ under visible-light irradiation. However, the DMPO-$\cdot O_2^-$ signal can hardly be observed for Bi_2S_3, possibly because the E_{CB} of Bi_2S_3 (–0.38 V *vs* NHE) is almost the same as the redox potential of $O_2/\cdot O_2^-$ and/or the electron-hole recombination is very severe in Bi_2S_3. The intensity of the DMPO-$\cdot O_2^-$ signal decreases greatly for CdS/Bi_2S_3-0.5h heterostructure compared with that of CdS, while it is still slightly stronger than that of Bi_2S_3, indicating that most of the photogenerated electrons in CdS can transfer to Bi_2S_3 in CdS/Bi_2S_3-0.5h heterostructure since the E_{CB} of Bi_2S_3 is much lower than that of CdS (–1.48 V, *vs* NHE). This conclusion can also be confirmed from the results of transient photocurrent response curves (Fig. S8), stead-state and time-resolved PL spectra (Fig. S9 and Table S2).

Interestingly, very different ESR results are obtained when measured in the presence of TEOA and FeTCPP under visible-light illumination (λ > 420 nm). A predominated signal with six peaks is observed for CdS (Fig. 7b), which can be assigned to DMPO-carbon centered radical (DMPO-C·) due to the oxidization of TEOA by the
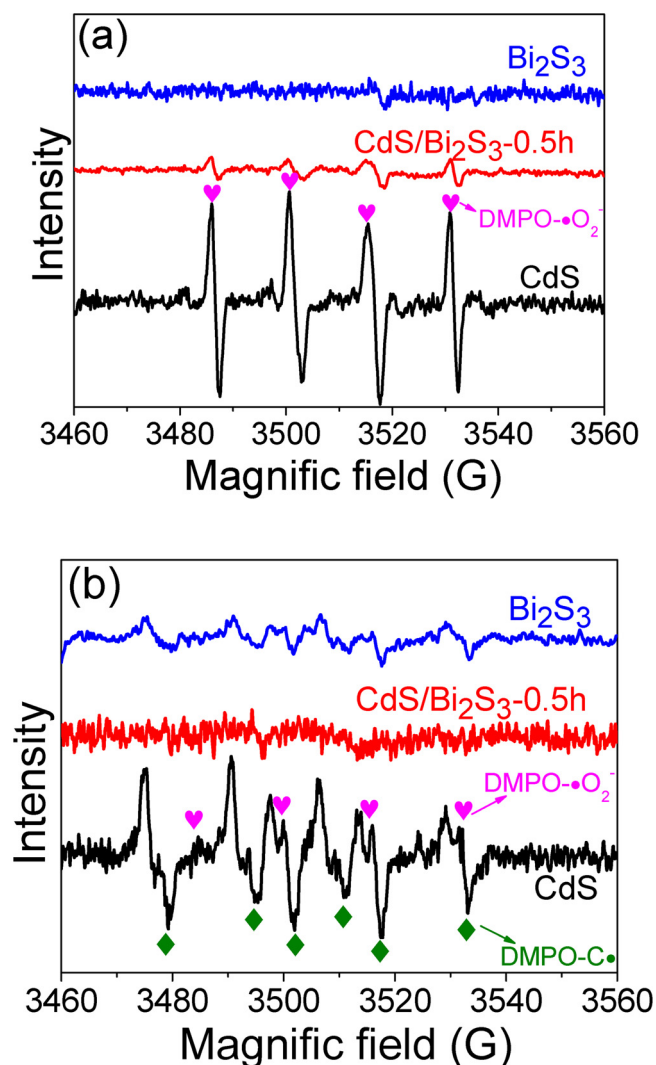
Fig. 7. ESR spectra of CdS, CdS/Bi$_2$S$_3$-0.5h and Bi$_2$S$_3$ using DMPO as radical scavenger under visible-light illumination (λ > 420 nm), (a) without FeTCPP and TEOA, (b) with FeTCPP and TEOA.

photogenerated holes in CdS [43,44]. However, no any ESR signal can be observed if the experiment was performed under the illumination of CdS with λ > 580 nm (Fig. S10), indicating that the DMPO-C· is formed from the oxidization of TEOA by the photogenerated holes in CdS. In addition to the DMPO-C· signal, the DMPO-·O$_2^-$ signal also appears for the CdS although it is very weak due to some reason not understood yet (Fig. 7b). Considering the strong DMPO-·O$_2^-$ signal for CdS in the case without the TEOA and FeTCPP (Fig. 7a), we infer that most of the photogenerated electrons in CdS can efficiently transfer to FeTCPP molecular catalyst due to the more negative E_{CB} of CdS and strong interaction between CdS and FeTCPP. The latter may be because of the carboxylic groups in the FeTCPP as they can coordinate with the Cd ions in CdS.

For Bi$_2$S$_3$ in the presence of TEOA and FeTCPP, no DMPO-·O$_2^-$ signal can be observed based on the same reason as discussed above. Furthermore, since the E_{CB} of Bi$_2$S$_3$ (–0.38 V) is less negative than that of FeTCPP (–1.02 V) and thus the electrons *cannot* transfer to FeTCPP, only a relatively weak DMPO-C· signal is observed for Bi$_2$S$_3$, which is originated from the oxidization of TEOA by the photogenerated holes in Bi$_2$S$_3$. The severe electron-hole recombination in Bi$_2$S$_3$ may explain the observed weak signal.

For CdS/Bi$_2$S$_3$-0.5 h in the presence of TEOA and FeTCPP, very interestingly, almost no ESR signal can be observed (Fig. 7b), while a

weak characteristic peak of DMPO-·O$_2^-$ can be observed without the TEOA and FeTCPP as mentioned above (Fig. 7a). Since the majority of electrons generated in the CB of CdS can transfer to the FeTCPP and the rest may transfer to the CB of Bi$_2$S$_3$ (Scheme 1), no DMPO-·O$_2^-$ signal can be observed in the ESR spectrum when there are TEOA and FeTCPP in the system. However, it is complicated for the behavior of holes. Those generated in the VB of Bi$_2$S$_3$ can either transfer to the VB of CdS or recombine directly with the electrons; whereas for the holes in the VB of CdS, no matter they are originally arisen from CdS or Bi$_2$S$_3$, considerable amount of them can recombine with the electrons transferred from the CB of Bi$_2$S$_3$ (*i.e.*, *via* Z-scheme mode, Scheme 1). Considering the DMPO-C· signal is very weak for both CdS and Bi$_2$S$_3$ in the presence of TEOA and FeTCPP, as well as the intrinsic recombination of both CdS and Bi$_2$S$_3$, no DMPO-C· signal can be detected either in the CdS/Bi$_2$S$_3$-0.5h when both TEOA and FeTCPP are present in the system.

Therefore, if the CdS/Bi$_2$S$_3$ is not hybrided with FeTCPP, it is thermodynamically favorable for the photogenerated electrons to migrate from the CB of CdS to that of Bi$_2$S$_3$ in the CdS/Bi$_2$S$_3$ heterostructure; meanwhile the electrons can also transfer from the CB of Bi$_2$S$_3$ to the VB of CdS through the Z-scheme mode. However, when the CdS/Bi$_2$S$_3$ is hybrided with FeTCPP, the photogenerated electrons in CdS will efficiently transfer to the FeTCPP, followed by the CO$_2$ reduction occuring over the FeTCPP molecular catalyst (Scheme 1). Accordingly, the electron transfer from CdS to Bi$_2$S$_3$ will be suppressed greatly upon intergration with FeTCPP. Therefore, the introduction of FeTCPP can change the transfer direction of electrons in CdS/Bi$_2$S$_3$-0.5 h heterostructure. More important, the strong reducibility of electrons in the CB of CdS can thus be preserved due to the feasibility of Z-scheme mode in the hybride catalyst, which is in favor of the transfer to FeTCPP. Meanwhile, the separation and utilization of charge carriers will be considerably enhanced. In addition, as discussed above, the reduced sulfur vacancy in the heterostructure can further faciliate the separation of charge carriers. As a result, CO$_2$ reduction can occur over the FeTCPP catalytic center much more efficiently, also because the TEOA acts as the sacrificial agent for hole scavenging.

4. Conclusions

In conclusion, we have successfully fabricated CdS/Bi$_2$S$_3$/FeTCPP heterogeneous hybrid photocatalysts for highly efficient photoreduction of CO$_2$ into CO and H$_2$ under visible-light irradiation. Here the semiconductor acts as the light-harvesting antenna and FeTCPP molecular catalyst works as the catalytic center for CO$_2$ reduction. The formation of CdS/Bi$_2$S$_3$ heterojunction can reduce the surface sulfur vacancy in CdS and thereby, increasing the charge separation and utilization. More important, the electron transfer direction can be changed once the CdS/Bi$_2$S$_3$ is integrated with the FeTCPP catalyst, as evidenced by the results of ESR and CO$_2$ reduction. Accordingly, CdS/Bi$_2$S$_3$-0.5 h/FeTCPP heterogeneous hybrid photocatalyst exhibits the highest activity for solar fuels production, with CO yield of 7.73 mmol/g and H$_2$ yield of 24.30 mmol/g after 4 h under visible-light irradiation. This work may afford a better understanding of CO$_2$ reduction over semiconductor heterostructure/molecular catalyst hybrid systems, and provide a feasible approach to fabricate highly efficient heterogeneous photocatalysts for solar fuel production.
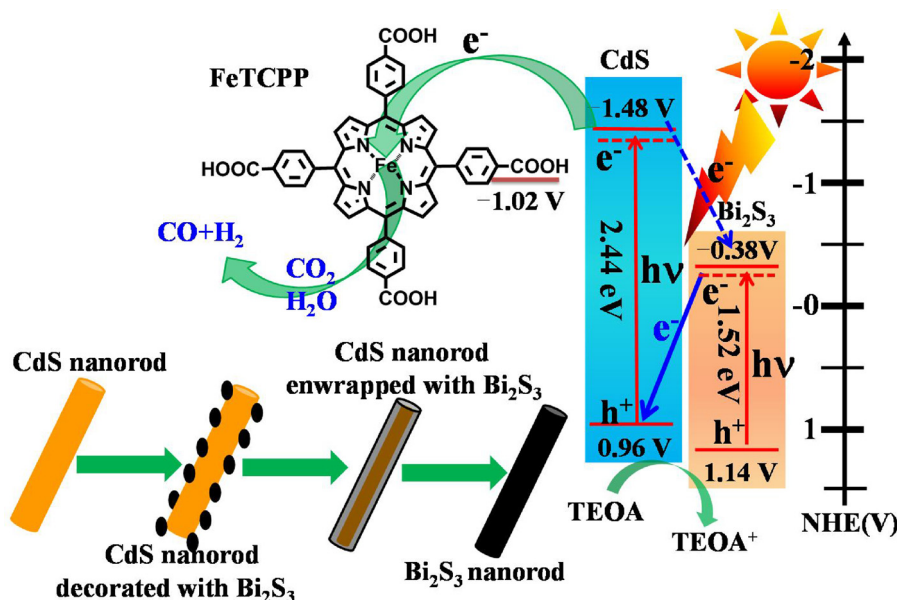
Scheme 1. Formation of CdS/Bi$_2$S$_3$ heterostructure and proposed charge transfer mechanism in CO$_2$ photoreduction over CdS/Bi$_2$S$_3$/FeTCPP hybrid catalysts under visible-light illumination. The dashed line indicates the suppressed electron transfer.

Appendix A. Supplementary data

Supplementary material related to this article can be found, in the online version, at doi:https://doi.org/10.1016/j.apcatb.2018.07.066.

References

[1] T. Inoue, A. Fujishima, S. Konishi, K. Honda, Nature 277 (1979) 637–638.
[2] S.N. Habisreutinger, L. Schmidt-Mende, J.K. Stolarczyk, Angew. Chem. Int. Ed. 52 (2013) 7372–7408.
[3] W.G. Tu, Y. Zhou, Z.G. Zou, Adv. Mater. 26 (2014) 4607–4626.
[4] J.L. White, M.F. Baruch, J.E. Pander III, Y. Hu, I.C. Fortmeyer, J. Eujin Park, T. Zhang, K. Liao, J. Gu, Y. Yan, T.W. Shaw, E. Abelev, A.B. Bocarsly, Chem. Rev. 115 (2015) 12888–12935.
[5] K. Li, B.S. Peng, T.Y. Peng, ACS Catal. 6 (2016) 7485–7527.
[6] S.J. Xie, Q.H. Zhang, G.D. Liu, Y. Wang, Chem. Commun. 52 (2016) 35–59.
[7] X.X. Chang, T. Wang, J.L. Gong, Energy Environ. Sci. 9 (2016) 2177–2196.
[8] L.J. Guo, Y.J. Wang, T. He, Chem. Rec. 16 (2016) 1918–1933.
[9] J.K. Stolarczyk, S. Bhattacharyya, L. Polavarapu, J. Feldmann, ACS Catal. 8 (2018) 3602–3635.
[10] G.H. Yin, X.Y. Huang, T.Y. Chen, W. Zhao, Q.Y. Bi, J. Xu, Y.F. Han, F.Q. Huang, ACS Catal. 8 (2018) 1009–1017.
[11] J.R. Ran, M. Jaroniec, S.Z. Qiao, Adv. Mater. 30 (2018) 1704649.
[12] A.J. Morris, G.J. Meyer, E. Fujita, Acc. Chem. Res. 42 (2009) 1983–1994.
[13] H. Takeda, O. Ishitani, Coordin. Chem. Rev. 254 (2010) 346–354.
[14] H. Takeda, C. Cometto, O. Ishitani, M. Robert, ACS Catal. 7 (2017) 70–88.
[15] T. Ouyang, H.H. Huang, J.W. Wang, D.C. Zhong, T.B. Lu, Angew. Chem. Int. Ed. 56 (2017) 738–743.
[16] F. Wen, C. Li, Acc. Chem. Res. 46 (2013) 2355–2364.
[17] X. Liu, S. Inagaki, J.G. Gong, Angew. Chem. Int. Ed. 55 (2016) 14924–14950.
[18] G.X. Zhao, H. Pang, G.G. Liu, P. Li, H.M. Liu, H.B. Zhang, L. Shi, J.H. Ye, Appl. Catal. B: Environ. 200 (2017) 141–149.
[19] S. Lian, M.S. Kodaimati, D.S. Dolzhnikov, R. Calzada, E. Weiss, J. Am. Chem. Soc. 139 (2017) 8931–8938.
[20] M.F. Kuehnel, K.L. Orchard, K.E. Dalle, E. Reisner, J. Am. Chem. Soc. 139 (2017) 7217–7223.
[21] Y. Xu, B. Zhang, Catal. Sci. Technol. 5 (2015) 3084–3096.
[22] Z.R. Tang, B. Han, C. Han, Y.J. Xu, J. Mater. Chem. A Mater. Energy Sustain. 5 (2017) 2387–2410.
[23] J.J. Zhao, Y.H. Li, P.F. Liu, Y.L. Wang, X.L. Du, X.L. Wang, H.D. Zeng, L.R. Zheng, H.G. Yang, Appl. Catal. B: Environ. 221 (2018) 152–157.
[24] W.L. Zhen, X.F. Ning, B.J. Yang, Y.Q. Wu, Z. Li, G.X. Lu, Appl. Catal. B: Environ. 221 (2018) 243–257.
[25] W.S. Jiang, X.P. Zong, L. An, S.X. Hua, X. Miao, S.L. Luan, Y.J. Wen, F.F. Tao, Z.C. Sun, ACS Catal. 8 (2018) 2209–2217.
[26] Q. Li, H. Meng, P. Zhou, Y.Q. Zheng, J. Wang, J.G. Yu, J.R. Gong, ACS Catal. 3 (2013) 882–889.
[27] T. Wu, X.G. Zhou, H. Zhang, X.H. Zhong, Nano Res. 3 (2010) 379–386.
[28] Z. Fang, Y.F. Liu, Y.T. Fan, Y.H. Ni, X.W. Wei, K.B. Tang, J.M. Shen, Y. Chen, J. Phys. Chem. C 115 (2011) 13968–13976.
[29] Y.H. Shi, Y.J. Chen, G.H. Tian, H.G. Fu, K. Pan, J. Zhou, H.J. Yan, Dalton Trans. 43 (2014) 12396–12404.
[30] X. Li, J. Chen, H. Li, J. Li, Y. Xu, Y. Liu, J. Zhou, J. Natural Gas Chem. 20 (2011) 413–417.
[31] C. Costentin, S. Drouet, M. Robert, J.M. Saveant, Science 338 (2012) 90–94.
[32] H. Rao, L.C. Schmidt, J. Bonin, M. Robert, Nature 548 (2017) 74–77.
[33] J. Bonin, M. Robert, M. Routier, J. Am. Chem. Soc. 136 (2014) 16768–16771.
[34] L. Lin, C.H. Hou, X.H. Zhang, Y.J. Wang, Y. Chen, T. He, Appl. Catal. B: Environ. 221 (2018) 312–319.
[35] G. Granados-Oliveros, E.A. Páez-Mozo, F.M. Ortega, C. Ferronato, J.-M. Chovelon, Appl. Catal. B: Environ. 89 (2009) 448–454.
[36] T.N. Knoxville, A.D. John, Lange's Handbook of Chemistry, 15th ed., McGraw-Hill, Inc, New York, 1999.
[37] H. Zhao, Y.M. Dong, P.P. Jiang, G.L. Wang, H.Y. Miao, R.X. Wu, L.G. Kong, J.J. Zhang, C. Zhang, ACS Sustain. Chem. Eng. 3 (2015) 969–977.
[38] S.R. Morrison, Electrochemistry at Semiconductor and Oxidized Metal Electrodes, Plenum Press, New York, 1980.
[39] J.L. Wang, Y. Yu, L.Z. Zhang, Appl. Catal. B: Environ 136–137 (2013) 112–121.
[40] J. Bonin, A. Maurin, M. Robert, Coord. Chem. Rev. 334 (2017) 184–198.
[41] Z. Fang, S. Weng, X. Ye, W. Feng, Z. Zheng, M. Lu, S. Lin, X.Z. Fu, P. Liu, ACS Appl. Mater. Interfaces 7 (2015) 13915–13924.
[42] H. Li, F. Qin, Z.P. Yang, X.M. Cui, J.F. Wang, L.Z. Zhang, J. Am. Chem. Soc. 139 (2017) 3513–3521.
[43] X.J. She, J.J. Wu, H. Xu, J. Zhong, Y. Wang, Y.H. Song, K.Q. Nie, Y. Liu, Y.C. Yang, M.T.F. Rodrigues, R. Vajtai, J. Lou, D.L. Du, H.M. Li, P.M. Ajayan, Adv. Energy Mater. 7 (2017) 1700025.
[44] D.C. Jiang, D. Chen, Z. Zhang, L. Zhang, Y. Wang, Z.J. Sun, R.M. Irfan, P.W. Du, J. Catal. 357 (2018) 147–153.